nuclei interacting with Ln^{3+} ions (in which case γ in eq 3 refers to the nucleus and r to the electron–nuclear distance). As part of an NMR study of lanthanide-bound micelles, we have measured the proton T_1 relaxation times for SDS micelles (0.07 M surfactant) to which a variety of Ln^{3+} ions (0.002 M) had been added.[22] The quantity of interest, plotted as hollow squares in Figure 1, is the relaxation enhancement for the CH_2 group in SDS bound directly to the sulfate, defined as $(1/T_1^{(L)}) - (1/T_1^{(0)})$, where $T_1^{(L)}$ and $T_1^{(0)}$ are the proton spin–lattice relaxation times in the presence and absence of lanthanide, respectively. (Gd^{3+} was not included because it produced line widths too broad to measure properly.) For Ln^{3+} ions the dipolar interaction typically dominates the Fermi contact term.[19,23] Note that the pattern of dipolar T_1 enhancements (hollow squares) does not match the pattern of k_e values (filled squares). This argues against a significant dipolar contribution to k_e.

(22) In this concentration regime T_1^{-1} was not linear with Ln^{3+} concentration. Therefore, all measurements were carried out at the same concentration.

(23) Alsaadi, B.; Rossotti, F.; Williams, R. *J. Chem. Soc., Chem. Commun.* **1980**, 2147.

Conclusion

We have measured bimolecular quenching rate constants k_e for interaction of lanthanide ions with the 1,9-biradical **2**. The evidence so far suggests that spin exchange is the principal quenching mechanism. The dipolar mechanism does not appear to have a major influence on the quenching. Further investigations, including the magnetic field dependence and chain length dependence of k_e, and lanthanide effect on intramolecular product ratios, are in progress.

Acknowledgment. The authors thank the National Science Foundation and Air Force Office of Scientific Research for support. C.D. thanks the NSF (CHE-84-21140) for support. K.C.W. thanks the National Institutes of Health for a postdoctoral fellowship, NCI-NIH No. CA07957.

A Realistic $HO_2(\tilde{X}^2A'')$ Potential Energy Surface from the Double Many-Body Expansion Method

A. J. C. Varandas,* J. Brandão, and L. A. M. Quintales†

Departamento de Química, Universidade de Coimbra, 3049 Coimbra Codex, Portugal
(Received: July 21, 1987; In Final Form: December 29, 1987)

A double many-body expansion potential energy surface reported previously for $HO_2(\tilde{X}^2A'')$ and referred to here as DMBE I is modified to produce thermal rate coefficients for the reaction $O + OH \rightarrow O_2 + H$ in good agreement with experiment. This new potential energy surface will be referred to as DMBE II. By the further imposition that the potential function should reproduce the experimental spectroscopic force field data for the hydroperoxyl radical, another potential energy surface has been obtained, DMBE III. Both of these improved DMBE II and DMBE III potential energy surfaces preserve the functional form used previously for DMBE I except for the long-range O···OH electrostatic interaction, which is defined in the spirit of a more satisfactory adiabatic theory.

1. Introduction

The potential energy surface for the electronic ground state of the hydroperoxyl radical, $HO_2(\tilde{X}^2A'')$, is important in understanding the chain-branching reaction (i) $H + O_2 \rightarrow OH + O$ of many combustion processes[1] and its reverse (ii) $O + OH \rightarrow O_2 + H$, both of which are also important in the HO_x cycle of atmospheric chemistry.[2,3] Connected with reactions (i) and (ii) are studies of isotope exchange[4] in O + OH and the vibrational relaxation[5] of O_2 in collisions with H. It is also important for theoretical studies of the vibrational–rotational spectroscopy of $HO_2(\tilde{X}^2A'')$ and, as a building block, for construction of the potential energy functions of larger polyatomics (which have ground-state HO_2 as a dissociation fragment) from the many-body expansion (MBE)[6] and double many-body expansion (DMBE)[7,8] methods. Thus, it is not surprising that there has been a considerable theoretical effort to arrive at a reliable potential energy surface for the electronic ground state of the hydroperoxyl radical, with use of both ab initio[9-14] and semiempirical[15-17] methods.

On the experimental side, the dissociation energy,[18,19] the geometry,[6,20,21] and the quadratic force constants[6,20] of the hydroperoxyl radical have also been reported. An extensive list of references to spectroscopic studies by a variety of techniques covering a wide range of the spectra can be found in ref 14.

Once a reliable three-dimensional (3D) working potential energy surface is available, it can be used for dynamics calculations by using either the classical trajectory method[4,5,22-29] or approximate quantum mechanical theories[30,31] and for variational transition

† Permanent address: Facultad de Química, Universidad de Salamanca, 37008 Salamanca, Spain.

(1) Benson, S. W.; Nangia, P. S. *Acc. Chem. Res.* **1979**, *12*, 223.
(2) Rowland, F. S.; Molina, M. *Rev. Geophys. Space Phys.* **1975**, *13*, 1.
(3) Lee, Y. P.; Howard, C. J. *J. Chem. Phys.* **1982**, *77*, 756.
(4) Miller, J. A. *J. Chem. Phys.* **1981**, *75*, 5349.
(5) Miller, J. A. *J. Chem. Phys.* **1981**, *74*, 5120.
(6) Murrell, J. N.; Carter, S.; Farantos, S. C.; Huxley, P.; Varandas, A. J. C. *Molecular Potential Energy Functions*; Wiley: Chichester, 1984.
(7) Varandas, A. J. C. *Mol. Phys.* **1984**, *53*, 1303.
(8) Varandas, A. J. C. *THEOCHEM* **1985**, *120*, 401.
(9) Melius, C. F.; Blint, R. J. *Chem. Phys. Lett.* **1979**, *64*, 183.
(10) Langhoff, S. R.; Jaffé, R. L. *J. Chem. Phys.* **1979**, *71*, 1475.
(11) Dunning, T. H., Jr.; Walch, S. P.; Wagner, A. C. In *Potential Energy Surfaces and Dynamics Calculations*; Truhlar, D. G., Ed.; Plenum: New York, 1981; p 329.
(12) Dunning, T. H., Jr.; Walch, S. P.; Goodgame, M. M. *J. Chem. Phys.* **1981**, *74*, 3482.
(13) Metz, J. Y.; Lievin, J. *Theor. Chim. Acta* **1983**, *62*, 195.
(14) Vazquez, G. J.; Peyerimhoff, S. D.; Buenker, R. J. *Chem. Phys.* **1985**, *99*, 239.
(15) Farantos, S. C.; Leisegang, E. C.; Murrell, J. N.; Sorbie, K. S.; Teixeira Dias, J. J. C.; Varandas, A. J. C. *Mol. Phys.* **1977**, *34*, 947.
(16) Gauss, A., Jr. *Chem. Phys. Lett.* **1977**, *52*, 252.
(17) Varandas, A. J. C.; Brandão, J. *Mol. Phys.* **1986**, *57*, 387.
(18) Howard, C. J. *J. Am. Chem. Soc.* **1980**, *102*, 6937. Foner, S. N.; Hudson, R. L. *J. Chem. Phys.* **1962**, *36*, 2681.
(19) Ogilvie, J. F. *Can. J. Spectrosc.* **1973**, *19*, 171.
(20) Beers, Y.; Howard, C. J. *J. Chem. Phys.* **1976**, *64*, 1541.
(21) Tuckett, R. P.; Freedman, P. A.; Jones, W. J. *Mol. Phys.* **1979**, *37*, 379, 403.
(22) Gauss, A., Jr. *J. Chem. Phys.* **1978**, *68*, 1689.

0022-3654/88/2092-3732$01.50/0

state[32] and adiabatic channel[33,34] treatments; ref 34 reports also simplified 1D short-range/long-range switching models for the radial and angular interaction O–OH potential in the context of the adiabatic channel model.

Ab initio electronic structure calculations of the ground-state HO_2 potential energy have been carried out by Melius and Blint,[9] Langhoff and Jaffé,[10] Dunning et al.,[11,12] Metz and Lievin,[13] and Vazquez et al.[14]; for references to earlier work see ref 9. Some of these articles[10,13,14] have also considered excited states of HO_2. Melius and Blint[9] carried out MCSCF CI calculations and defined a global HO_2 surface by fitting the calculated points to an ad hoc functional form. This surface gives a barrier of about 2.3 kcal mol^{-1} for the H + O_2 addition reaction. Using a more extensive CI wave function, Langhoff and Jaffé[10] reported no barrier for this addition step. Dunning et al.[11,12] carried out generalized valence bond calculations and concluded that by taking the computational deficiencies into account, it is likely that there is no barrier to the addition reaction. Metz and Lievin[13] and Vazquez et al.[14] concentrate on the electronic spectra and UV photodissociation of HO_2 and hence do not address this barrier problem on the ground-state potential surface of HO_2.

In a recent article[17] (hereafter referred to as article I), we reported a potential energy surface for $HO_2(\tilde{X}^2A'')$ using the DMBE method. This HO_2 DMBE I potential surface conforms with the ab initio data of Melius and Blint[9] for the three-body energy and shows reasonable agreement with available spectroscopic data for the energy and geometry of the minima referring to the equilibrium triatomic. In agreement with the best ab initio estimates, it also shows no barrier for the H + $O_2 \rightarrow$ OH + O reaction. In addition, the HO_2 DMBE I potential energy surface predicts two secondary minima that have chemical interest. One refers to a T-shaped (C_{2v}) H–O_2 weakly bound complex, while the other is related to a linear ($C_{\infty v}$) weak hydrogen-bonded O···HO structure. Moreover, it shows the appropriate long-range behavior of the H–O_2 and O–OH asymptotic channels being the electrostatic energy defined in the spirit of an adiabatic theory recently proposed by Clary and Werner.[31] This is particularly significant since Clary[30,31] has shown that the long-range forces are major factors in determining the rate constant for the O + OH $\rightarrow$ O_2 + H reaction. Such importance has most recently been stressed by Troe[34] in his statistical adiabatic channel model. Along the same direction, Wagner[35] has explicitly considered coupling between the long-range O + OH spin–orbit potential curves.

Despite the fact that the HO_2 DMBE I potential energy surface shows some definite improvement over previous functions, it is not completely satisfactory. For example, exploratory trajectory results[29] for the O + OH $\rightarrow$ O_2 + H reaction have yielded thermal rate coefficients that significantly underestimate the best available experimental measurements (for a critical review, see ref 36). In contrast, similar calculations carried out on the Melius–Blint fit[9] agree well[28] with the experimental results. The aim of this work is therefore to report a new DMBE potential energy surface for $HO_2(\tilde{X}^2A'')$ that overcomes such difficulty. In addition we suggest an alternative, perhaps more satisfactory, adiabatic description of the long-range O–OH electrostatic interaction. Finally, we show how to make the potential reproduce the complete quadratic force field of the hydroperoxyl radical as surveyed in ref 6 and 21, while maintaining a good description of the rate coefficient measurements for the O + OH $\rightarrow$ O_2 + H reaction.

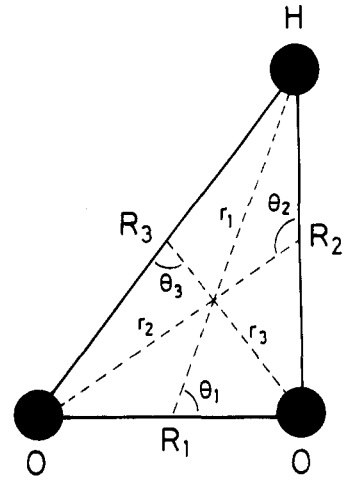

Figure 1. Coordinates used to define the HO_2 potential energy surface.

This article is organized as follows: Section 2 outlines the mathematical form of the energy terms in the DMBE and describes the approach used to obtain the numerical values of the parameters they contain from available ab initio[9] and spectroscopic[6,21] data. Section 3 presents a discussion of the results. The conclusions are gathered in section 4.

2. New DMBE HO_2 Potentials

The DMBE of the potential energy for ground-state HO_2 has the form[37,38]

$$V = V_{EHF}(R) + V_{corr}(R) \tag{1}$$

where EHF denotes an extended-Hartree–Fock-type energy that includes the nondynamical correlation due to degeneracies or near-degeneracies of the valence orbitals, and corr is the dynamical correlation energy due to the true dynamic correlation of the electrons; $R = R_1, R_2, R_3$ is a collective variable of the internuclear separations, which are defined in Figure 1. In eq 1, both the EHF and corr energy terms are written as a many-body expansion:[6]

$$V_{EHF}(R) = \sum_{i=1}^{3} V^{(2)}_{EHF,i}(R_i) + V^{(3)}_{EHF}(R_1,R_2,R_3) \tag{2}$$

$$V_{corr}(R) = \sum_{i=1}^{3} V^{(2)}_{corr,i}(R_i) + V^{(3)}_{corr}(R_1,R_2,R_3) \tag{3}$$

where all two-body and three-body fragments are assumed to be in their ground-electronic states as predicted from the Wigner–Witmer spin–spatial correlation rules; $i = 1$ is taken to label the homonuclear OO bond, and $i = 2$ and 3 label the two OH bonds. A detailed review of the theory has been given elsewhere[8,37,38] and will not be repeated here. Instead, we refer only to those aspects that are essential for this work. The notation is mainly that of article I; for further clarity, we use the initials EHF[37,38] rather than HF[7,8,17] to represent the extended-Hartree–Fock-type energy.

In article I the two-body energy terms assumed the form of the realistic EHFACE model[39] and are thus kept unchanged in the current work. They have the general form

$$V^{(2)}_{EHF}(R) = DR^{\alpha}(1 + \sum_{i=1}^{3} a_i r^i) \exp(-\gamma r) \tag{4}$$

$$V^{(2)}_{corr}(R) = -\sum_{n=6,8,10} C_n \chi_n(R) R^{-n} \tag{5}$$

where $r = R - R_m$ is the displacement coordinate from the equilibrium diatomic geometry. In eq 5, χ_n are dispersion damping

(23) Blint, R. J. *J. Chem. Phys.* **1980**, *73*, 765.
(24) Bottomley, M.; Bradley, J. N.; Gilbert, J. R. *Int. J. Chem. Kinet.* **1981**, *13*, 957.
(25) Gallucci, C. S.; Schatz, G. C. *J. Phys. Chem.* **1982**, *86*, 2352.
(26) Brown, N. J.; Miller, J. A. *J. Chem. Phys.* **1984**, *80*, 5568.
(27) Kleinermanns, K.; Schinke, R. *J. Chem. Phys.* **1984**, *80*, 1440.
(28) Miller, J. A. *J. Chem. Phys.* **1986**, *84*, 6170.
(29) Quintales, L. A. M.; Varandas, A. J. C.; Alvariño, J. M. *J. Phys. Chem.*, in press.
(30) Clary, D. C. *Mol. Phys.* **1984**, *53*, 3.
(31) Clary, D. C.; Werner, H. J. *Chem. Phys. Lett.* **1984**, *112*, 346.
(32) Rai, S. N.; Truhlar, D. G. *J. Chem. Phys.* **1983**, *79*, 6046.
(33) Cobos, C. J.; Hippler, H.; Troe, J. *J. Phys. Chem.* **1985**, *89*, 342.
(34) Troe, J. *J. Phys. Chem.* **1986**, *90*, 3485.
(35) Wagner, A., private communication.
(36) Cohen, N.; Westberg, K. R. *J. Phys. Chem. Ref. Data* **1983**, *12*, 531.
(37) Varandas, A. J. C. In *Structure and Dynamics of Weakly Bound Complexes*; Weber, A., Ed.; D. Reidel: Dordrecht, 1987; p 357.
(38) Varandas, A. J. C. *Adv. Chem. Phys.*, in press.
(39) Varandas, A. J. C.; Dias da Silva, J. *J. Chem. Soc., Faraday Trans. 2* **1986**, *82*, 593.

TABLE I: Coefficients Used for the Ground-State O_2 and OH Potentials[a]

coeff	O_2	OH
$-D$	0.14291	0.13825
a_1	3.64459	2.65648
a_2	3.92812	1.74505
a_3	2.09867	0.71014
γ	3.35225	2.54533
α	0	0
R_0[b]	5.66169	6.29489
R_m	2.2818	1.8344
C_6	15.40	10.00
C_8	235.22	180.45
C_{10}	4066.24	3685.26

[a] Calculated from equations 4 and 5; see also text. All values are in atomic units. [b] Calculated from eq 6a with $\langle r_H^2 \rangle = 3a_0^2$ and[43] $\langle r_O^2 \rangle = 2.00\,43 a_0^2$.

TABLE II: Coefficients for the Three-Body Correlation Energy[a]

OH bond[b,c]		
$k_6 = 2.46501\ (-2)$	$k_8 = 5.03696\ (-2)$	$k_{10} = 6.29438\ (-2)$
$\eta_6 = k'_6 = 0.68758$	$\eta_8 = k'_8 = 0.82542$	$\eta_{10} = k'_{10} = 0.94034$
OO bonds[b,d]		
$k_6 = -2.78478\ (-1)$	$k_8 = -4.68155\ (-1)$	$k_{10} = -1.20507\ (0)$
$\eta_6 = k'_6 = 0.95274$	$\eta_8 = k'_8 = 0.94148$	$\eta_{10} = k'_{10} = 0.72379$

[a] Calculated from eq 7; units are as in Table I. Given in parentheses are the powers of 10 by which the numbers should be multiplied, e.g., $2.465\,01\ (-2) = 2.465\,01 \times 10^{-2}$. [b] η'_n ($n = 6, 8, 10$) are taken equal to unity for all diatomic fragments. [c] $R^\circ = 1.8344\ a_0$. [d] $R^\circ = 2.2818\ a_0$.

functions (for recent references to earlier work on dispersion damping see ref 38 and 40) defined by[8,41]

$$\chi_n(R) = [1 - \exp(-(A_n R/\rho) - (B_n R^2/\rho^2))]^n \quad (6a)$$

where

$$A_n = \alpha_0 n^{-\alpha_1} \quad (6b)$$

$$B_n = \beta_0 \exp(-\beta_1 n) \quad (6c)$$

$$\rho = (R_m + 2.5R_0)/2 \quad (6d)$$

$$R_0 = 2(\langle r_X^2 \rangle^{1/2} + \langle r_Y^2 \rangle^{1/2}) \quad (6e)$$

is the Le Roy[42] distance for the onset of breakdown of the asymptotic R^{-n} perturbation series expansion, X and Y label the two interacting atoms, $\langle r_X^2 \rangle$ and $\langle r_Y^2 \rangle$ are the corresponding expectation values for the squared radii of the outer orbitals of X and Y, and α_i and β_i ($i = 0, 1$) are dimensionless universal constants[8] for all isotropic interactions: $\alpha_0 = 25.9528$, $\alpha_1 = 1.1868$, $\beta_0 = 15.7381$, and $\beta_1 = 0.09729$. (Unless mentioned otherwise, all values reported are in atomic units: 1 hartree (E_h) = 1 au of energy = 4.359 821 5 aJ; 1 bohr (a_0) = 1 au of length = 0.529 177 Å = 0.052 917 7 nm.) Table I defines the numerical values of the coefficients in eq 4–6 for the OH($\tilde{X}^2\Pi$) and $O_2(\tilde{X}^3\Sigma^-_g)$ diatomic fragments.

Also the three-body dynamical correlation energy, which is calculated semiempirically within the DMBE framework, is defined as in article I. It is written as[37,38,44]

$$V^{(3)}_{corr}(R) = \sum_{i=1}^{3} \sum_{n=6,8,10} C_n \chi_n(R_i)\{1 - \tfrac{1}{2}[g_n(R_{i+1(\mathrm{mod}\,3)}) \times h_n(R_{i+2(\mathrm{mod}\,3)}) + g_n(R_{i+2(\mathrm{mod}\,3)})\, h_n(R_{i+1(\mathrm{mod}\,3)})] R_i^{-n}\} \quad (7a)$$

where

$$g_n(R_i) = 1 + k_n^{(i)} \exp[-k'^{(i)}_n (R_i - R_i^\circ)] \quad (7b)$$

$$h_n(R_i) = [\tanh(\eta_n^{(i)} R_i)]^{\eta'^{(i)}_n} \quad (7c)$$

and R_i° is a reference geometry; for the numerical values of the coefficients in eq 7, see Table II.

TABLE III: Coefficients for the Three-Body Electrostatic Energy Term[a]

OH bonds[b]	$K_4 = K_5 = 0.08831$[c]	$K'_4 = K'_5 = \eta_4 = \eta_5 = 2.54533$
OO bond[b]	$K_4 = K_5 = 0.0$	$k'_4 = K'_5 = \eta_4 = \eta_5 = 3.35225$

[a] Calculated from eq 8, with $\xi = 4$; all quantities are in atomic units. [b] η'_n ($n = 4, 5$) are taken equal to unity for all diatomic fragments. [c] $K_4 = K_5 = (1/R^\circ)^4$ with $R^\circ = R_m = 1.8344\ a_0$.

Modifications that lead to the improved DMBE potentials of the current work refer therefore only to the three-body EHF energy term and to the description of the O–OH electrostatic energy, which is treated[17] separately from the rest of the three-body EHF term. We therefore begin our discussion with this electrostatic energy term.

2.1. Three-Body Electrostatic Energy. As in previous work,[17,38] the three-body electrostatic energy term is similarly represented by

$$V^{(3)}_{ele}(R) = \tfrac{1}{2}\sum_{i=1}^{3} \sum_{n=4,5} [C_n G_n(R_{i+1(\mathrm{mod}\,3)})\, h_n(R_{i+2(\mathrm{mod}\,3)}) + C'_n G_n(R_{i+2(\mathrm{mod}\,3)})\, h_n(R_{i+1(\mathrm{mod}\,3)})]\, \chi_n(R_i) R_i^{-n} \quad (8a)$$

where ele stands for electrostatic

$$G_n(R_i) = K_n R_i^\xi \exp[-K'^{(i)}_n (R_i - R_i^\circ)] \quad (8b)$$

and h_n is defined by eq 7c. Note that C_n represents the long-range electrostatic coefficient for the atom–diatom interaction involving the $i + 1(\mathrm{mod}\,3)$ diatomic and the remaining atom of the ith pair (that associated with R_i), and C'_n has a similar meaning but refers to the other atom of the ith pair with the $i + 2(\mathrm{mod}\,3)$ diatomic. Similarly, χ_n denotes the damping function of order n for the ith diatomic fragment, which has been defined by eq 6a. Since there is no H–OO long-range electrostatic interaction, one must have $G_n(R_1) = 0$; see Table III.

As for the K_n and K'_n coefficients, they are determined from the requirement that given values for η_n and η'_n, $V^{(3)}_{ele}$ should reproduce the long-range electrostatic energy that results from the interaction between the permanent quadrupole moment (Θ_a) of the O atom and the dipole (μ_b) and quadrupole (Θ_b) moments of OH; a labels the O center, while b stands for the center of mass of OH. Note that the quadrupole–dipole interaction (Θ_a–μ_b) leads to an energy contribution that varies as $C_4 r^{-4}$, while that for the quadrupole–quadrupole (Θ_a–Θ_b) interaction varies as $C_5 r^{-5}$, where C_4 and C_5 are defined by[45]

$$C_4 = \tfrac{3}{4}\Theta_a \mu_b [\cos\theta_b (3\cos^2\theta_a - 1) - 2\sin\theta_a \sin\theta_b \cos\theta_a \cos\phi_{ab}] \quad (9)$$

$$C_5 = \tfrac{3}{16}\Theta_a\Theta_b (1 - 5\cos^2\theta_a - 5\cos^2\theta_b + 17\cos^2\theta_a \cos^2\theta_b + 2\sin^2\theta_a \sin^2\theta_b \cos^2\phi_{ab} - 16\sin\theta_a \sin\theta_b \cos\theta_a \cos\theta_b \cos\phi_{ab}) \quad (10)$$

where r is the O–OH center-of-mass separation, θ_a and θ_b are the angles made by the axis of the electric multipole moments with r, and ϕ_{ab} is the dihedral angle between those axes; in the present calculations, the electric multipole moments for the O atom and OH diatomic are given the values[46] $\Theta_a = -1.60\ ea_0^2$ and[47] $\mu_b = 0.656\ ea_0$ and[48] $\Theta_b = 1.37\ ea_0^2$, respectively. Note especially that the C_4 and C_5 coefficients depend on the atom–diatom orientation though they vanish when averaged (for a fixed atom–center of mass of the diatomic separation) over the angles θ_a, θ_b, and $\phi_{ab} = \phi_a - \phi_b$.[45]

To define C_4 and C_5, we have, in article I, followed the adiabatic theory of Clary and Werner,[31] which constrains the angle θ_a at $\theta_a = 0$ such as to give the lowest value for the dipole–quadrupole and quadrupole–quadrupole electrostatic energies. However, Clary's approach assumes that the quadrupole axis of the O atom always lies along the vector connecting the atom to the center of

(40) Knowles, P. J.; Meath, W. J. *Mol. Phys.* **1987**, *60*, 1143.
(41) Varandas, A. J. C.; Brandão, J. *Mol. Phys.* **1982**, *45*, 857.
(42) Le Roy, R. J. *Mol. Spectrosc. Chem. Soc. (London)* **1973**, *1*, 113.
(43) Desclaux, J. P. *At. Data* **1973**, *12*, 311.
(44) Varandas, A. J. C.; Brown, F. B.; Mead, C. A.; Truhlar, D. G.; Blais, N. C. *J. Chem. Phys.* **1987**, *86*, 6258.
(45) Hirschfelder, J. O.; Curtiss, C. F.; Bird, R. B. *The Molecular Theory of Gases and Liquids*, 2nd ed.; Wiley: New York, 1964.
(46) Fisher, C. F. *At. Data* **1973**, *12*, 87.
(47) Meerts, W. L.; Dymanus, A. *Chem. Phys. Lett.* **1973**, *23*, 45.
(48) Chu, S. I.; Yoshimine, M.; Liu, B. *J. Chem. Phys.* **1974**, *61*, 5389.

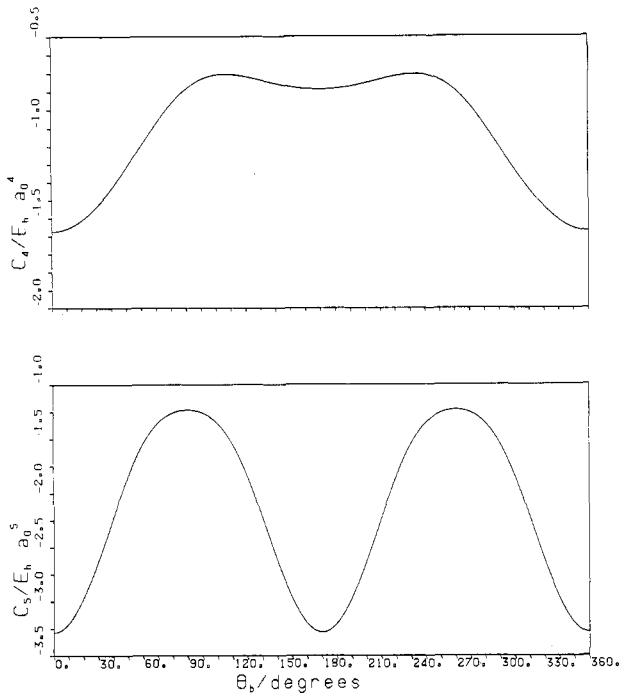

Figure 2. Optimum values of the C_4 and C_5 O–OH long-range electrostatic coefficients as a function of the angle θ_b (this may be either θ_2 or θ_3 in the notation of Figure 1), the angle formed by the OH axis with the line connecting the remaining O atom with the center of mass of OH. The three-term Fourier analysis of eq 11 is essentially indistinguishable within the scale of the figure, and hence it is not shown.

TABLE IV: Values of the Expansion Coefficients in the Fourier Series Analysis of Eq 11[a]

parameter	c_4^{opt}	c_5^{opt}
b_0	−1.987 67	−4.290 02
b_1	−0.393 61	0[b]
b_2	−0.195 76	−1.043 70
b_3	0[b]	0[b]
b_4	0.009 78	−0.115 02
b_5	0[b]	0[b]
b_6	−0.000 94	0.016 72
max. dev (three terms), %	1.1	1.7
max. dev (four terms), %	0.1	0.1

[a] Units are $E_h a_0^4$ and $E_h a_0^5$ for C_4 and C_5, respectively. [b] Smaller in absolute value than 0.0001 au.

mass of the OH molecule. As a result, there is a change of sign of the potential as the angle of approach of the O atom changes from head on with the O end of OH to head on with the H end of OH.

A more satisfactory adiabatic description of the long-range electrostatic interaction is to let the electronic distribution on the O atom instantaneously adjust to the OH electronic charge distribution, whatever the angle θ_b of approach, so as to produce the lowest potential energy. We will follow this approach in the present work. Since a quadrupole can be thought of as having one charge on each corner of a square with the charges alternating in sign around the square, this would correspond to a change in its angle of approach by 180°. Thus, the negatively charged diagonal axis of the quadrupole square will be coincident with the OH axis when O approaches the H end of OH, but the positively charged diagonal will be coincident if the O end is approached. We choose therefore, for a fixed value of θ_b, the value of θ_a that gives the lowest interaction potential energy. Figure 2 shows the optimum values of C_4 and C_5 obtained from this procedure. They can be described in terms of a Fourier expansion:

$$C_n^{opt} = (b_0/2) + \sum_{j=1}^{N} b_j \cos(j\theta_b) \qquad (11)$$

where the coefficients for $N = 6$ are given in Table IV. Note

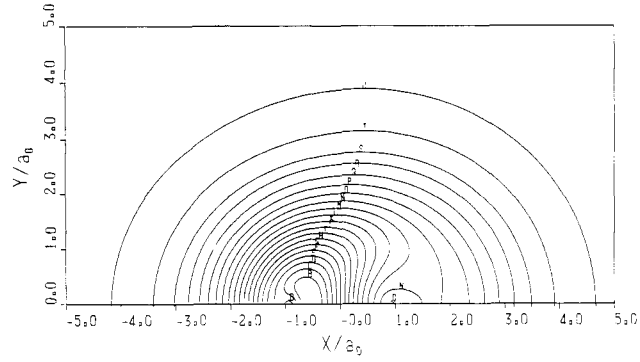

Figure 3. Contours of the electrostatic energy, eq 8, for an O atom moving around an equilibrium OH with the center of mass fixed at the origin. Contours are equally spaced by 0.01 E_h starting at $A = -0.20$ E_h.

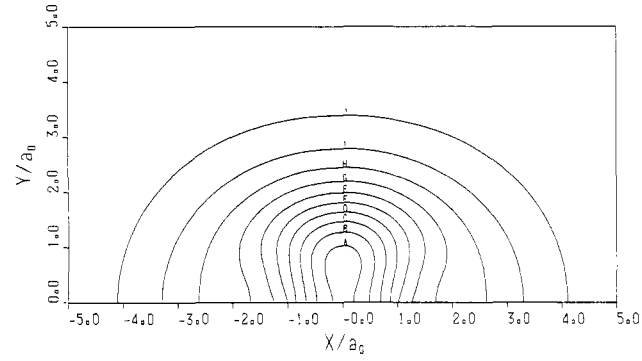

Figure 4. Same as in Figure 3 but for a H atom moving around an equilibrium O_2.

that sine terms in the Fourier series expansion vanish due to symmetry reasons. Note especially that a three-term Fourier analysis reproduces the calculated data within 1–2% and that a conversion to the (R_1,R_2,R_3) set of coordinates can be made by using the pseudoangular coordinate reported in eq 11 of article I; see also ref 38. However, rather than using C_n^{opt}, we adopt a simpler approach that is similar to that employed for the dispersion coefficients.[8,37,38] Accordingly, we parametrize eq 8 so as to reproduce the spherically averaged values of these optimum long-range coefficients for the O···OH electrostatic interaction energy. To perform numerically the sine-weighted θ_b averaging, we have used a Gauss–Legendre quadrature technique, having obtained $\langle C_4 \rangle = -0.929 E_h a_0^4$ and $\langle C_5 \rangle = -1.790 E_h a_0^5$.

Figure 3 shows contours of the electrostatic energy, as predicted from eq 8, for an O atom moving around an equilibrium OH diatomic. A similar contour plot for the H atom moving around an equilibrium O_2 is shown in Figure 4. In contrast to the electrostatic energy from article I that shows, as a polar plot in O–OH radial distance and angle of approach, a sign change at the line corresponding approximately to a 90° insertion of O into the middle of OH, the current approach produces long-range electrostatic potentials that are attractive at every angle of approach though they are least attractive for the perpendicular insertion of O into OH.

Although the change of sign in C_4 and C_5 of article I might affect the dynamics at low collision energies, it is hardly expected from the magnitude of the energies involved that this sign change may significantly alter the dynamics at high energies. Indeed, exploratory dynamics studies[29] on the HO_2 DMBE I potential energy surface have shown that a small energy barrier along the minimum energy path for the $O + OH \rightarrow O_2 + H$ reaction was responsible for the poor agreement between the calculated thermal rate coefficients and experiment.[36,49–51] This barrier, which also

(49) Lewis, R. S.; Watson, R. T. *J. Phys. Chem.* **1980**, *84*, 3495.
(50) Howard, M. J.; Smith, I. W. M. *J. Chem. Soc., Faraday Trans. 2* **1981**, *77*, 997.
(51) Deleted in proof.
(52) Frank, P.; Just, Th. *Ber. Bunsen-Ges. Phys. Chem.* **1985**, *89*, 181.

appears on the O–OH spherically averaged interaction energy curve, must therefore be removed. For this purpose a further least-squares fit to the three-body ab initio EHF energies has been carried out as described in the following subsection.

2.2. Nonelectrostatic Three-Body EHF Energy. As in article I, the remainder of the three-body EHF energy assumes the form

$$V_{EHF'}^{(3)} = V^{\circ}(1 + c_1Q_1 + c_2Q_3 + c_3Q_1^2 + c_4S_{2a}^2 + c_5Q_1Q_3 + c_6S_{2b}^2 + c_7Q_1^3 + c_8Q_1S_{2a}^2 + c_9S_3^3 + c_{10}Q_1^2Q_3 + c_{11}Q_1S_{2b}^2 + c_{12}Q_3S_{2a}^2 + c_{13}Q_1^4 + c_{14}Q_1^2S_{2a}^2 + c_{15}S_{2a}^2 + c_{16}Q_1S_3^3 + c_{17}Q_1^3Q_3 + c_{18}Q_1^2S_{2b}^2 + c_{19}Q_1Q_3S_{2a}^2 + c_{20}Q_3S_3^3 + c_{21}S_{2a}^2S_{2b}^2 + c_{22}Q_1^5 + c_{23}Q_1^3S_{2a}^2 + c_{24}Q_1S_{2a}^4 + c_{25}Q_1^2S_3^3 + c_{26}S_{2a}^2S_3^3 + c_{27}Q_1^4Q_3 + c_{28}Q_1^3S_{2b}^2 + c_{29}Q_1^2Q_3S_{2a}^2 + c_{30}Q_1Q_3S_3^3 + c_{31}Q_1S_{2a}^2S_{2b}^2 + c_{32}Q_3S_{2a}^4 + c_{33}S_{2b}^2S_3^3)\prod_{i=1}^{3}\{1 - \tanh[\gamma_0^{(i)} + \gamma_1^{(i)}R_i]\} \quad (12)$$

where the prime denotes that the electrostatic energy is left out, and Q_i (i = 1–3) are the D_{3h} symmetry coordinates defined by

$$\begin{bmatrix} Q_1 \\ Q_2 \\ Q_3 \end{bmatrix} = \begin{bmatrix} 1/3^{1/2} & 1/3^{1/2} & 1/3^{1/2} \\ 0 & 1/2^{1/2} & -1/2^{1/2} \\ 2^{1/2}/3^{1/2} & -1/6^{1/2} & -1/6^{1/2} \end{bmatrix} \begin{bmatrix} R_1 \\ R_2 \\ R_3 \end{bmatrix} \quad (13)$$

$$S_{2a}^2 = Q_2^2 + Q_3^2 \quad (14a)$$

$$S_{2b}^2 = Q_2^2 - Q_3^2 \quad (14b)$$

$$S_3^3 = Q_3^3 - 3Q_2^2Q_3 \quad (14c)$$

Also as in article I we define $\gamma_0^{(i)} = -\gamma_1^{(i)}R_i^{ref}$, where R_i^{ref} (i = 1–3) is a reference C_{2v} geometry defined through the experimental equilibrium HO_2 geometry (denoted R_i^e (i = 1–3); note that the latter differs slightly numerically from that used in ref 17) as follows: $R_1^{ref} = R_1^e$ and $R_2^{ref} = R_3^{ref} = (R_2^e + R_3^e)/2$. Moreover, the value of $\gamma_1^{(1)}$ has been taken from the nonlinear least-squares fit carried out in article I, while those of $\gamma_1^{(2)} = \gamma_1^{(3)}$ have been obtained through a trial-and-error procedure by carrying out linear least-squares fits (the least-squares parameters being V° and c_i, with i = 1–33) to the remainder three-body energies which are obtained by subtracting the sum of the three-body dynamical correlation energy (see ref 17) and the three-body electrostatic energy from the three-body correlated ab initio energies of Melius and Blint.[9] (Although the ab initio surface of Melius and Blint gives inaccurate dissociation energies and hence is questionable for dynamics studies, we believe[17] that due to a cancellation of errors the ab initio three-body energy contributions have greater reliability. By combining the latter with accurate semiempirical curves for the diatomic fragments, one should therefore get an improved description of the complete triatomic potential energy surface.) Thus, least-squares fits to the 365 data points so obtained have been generated until no nonphysical minima appeared in the final potential energy function, and the corresponding barrier in the O + OH minimum energy reaction path (or alternatively in the spherically averaged component V_0 of the O–OH interaction potential; see later) was below the O + OH dissociation limit; see Figure 5. Note that this barrier separates the shallow minimum associated with the O···HO hydrogen-bonded structure from the deep chemical minimum corresponding to equilibrium HO_2. In our previous HO_2 DMBE I potential the minimum associated with this O···HO hydrogen-bonded structure was separated from the deep HO_2 chemical well by an energy barrier of at least 0.13 kcal mol^{-1} (relative to O + OH) located at $R_1 = 4.60a_0$, $R_2 = 1.84a_0$, $R_3 = 4.63a_0$.

A simple way to remove the positive barrier in the O + OH minimum energy reaction path has been to allow small adjustments into the β_{OO} and β_{OH} range-determining parameters of the two-body Morse potentials used by Melius and Blint[9] (which are then subtracted from the HO_2 energies to calculate the three-body ab initio energies) while $\gamma_1^{(2)} = \gamma_1^{(3)}$ were varied freely as discussed above to yield the best least-squares fit. To improve the reliability of our prediction at the equilibrium geometry of the hydroperoxyl radical, we considered a least-squares weight function in fitting the nonelectrostatic three-body residual EHF energies, namely, $W = 1 + 99\exp[\tilde{g}((R_1 - R_1^e)^2 + (R_2 - R_2^e)^2 + (R_3 - R_3^e)^2)]$; see Table V. Note that the diatomic Morse parameters (β_{OO} and β_{OH}) were not specified by Melius and Blint[9] for the ab initio energies, and we adopted, somewhat arbitrarily, the values $\beta_{OO} = 1.45a_0^{-1}$ and $\beta_{OH} = 1.38a_0^{-1}$ in article I. To reduce the current least-squares fitting procedure to a two-variable trial-and-error search, we have forced the β_{OO}/β_{OH} ratio to be equal to that[53]

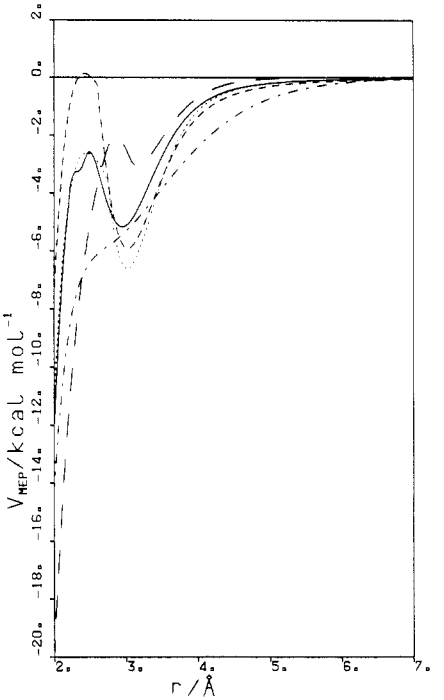

Figure 5. Potential along the minimum energy reaction path as a function of the separation, in angstroms, between the O atom and the center of mass of OH: (–·–) Melius–Blint[9] potential surface; (– – –) MBE[15] potential surface; (·–·) DMBE I[17] potential surface; (···) this work DMBE II potential surface; (—) this work DMBE III potential surface.

TABLE V: Weights Used for the Least-Squares Fitting Procedures Related to the HO_2 DMBE Potentials of This Work[a]

DMBE II
ab initio points (i = 1–365):
$W_i = 1 + 99\exp[-100\sum_{i=1}^{3}(R_i - R_i^e)^2]$
special point

no.	R_1	R_2	R_3	V	wt
366	5.521 810	1.906 955	3.614 856	−0.178 168	100[b]

DMBE III
ab initio points (i = 1–365):
$W_i = 1 - \exp[-100\sum_{i=1}^{3}(R_i - R_i^e)]^2$
special points

no.	R_1	R_2	R_3	V	wt
366	5.521 810	1.906 955	3.614 856	−0.178 168	10[b]
367	2.512	1.843	3.457	−0.27 47	1000[c]
368	1.85	1.834 4	0.99	0.34 097	1[d]
369	2.226 492	4.542 893	4.542 893	−0.20 1568	1000[d]
370	2.283 606	7.263 427	7.263 427	−0.19 2700	1000[d]
371–373	2.512	1.843	3.457	1st der	10000[e]
374–379	2.512	1.843	3.457	2nd der	$10/F_{ij}^{2}$[f]

[a] Units are as in Table I. [b] OH···O hydrogen-bonded structure. [c] Experimental binding energy of HO_2.[6,18–21] [d] Estimated energy from the HO_2 DMBE II potential surface of the present work. [e] Condition of zero first derivative at the equilibrium geometry of HO_2. [f] Condition to impose the quadratic force constants of HO_2: $F_{11} = \partial^2V/\partial R_2^2$; $F_{22} = \partial^2V/\partial R_2^2$; $F_{\alpha\alpha} = \partial^2V/\partial\alpha^2$; $F_{12} = \partial^2V/\partial R_1\partial R_2$; $F_{1\alpha} = \partial^2V/\partial R_1\partial\alpha$; $F_{2\alpha} = \partial^2V/\partial R_2\partial\alpha$.

(53) Huber, K. P.; Herzberg, G. *Molecular Spectra and Molecular Structure: Constants of Diatomic Molecules*; van Nostrand: New York, 1979.

TABLE VI: Coefficients for the Residual Three-Body Extended-Hartree-Fock Energy Term[a,b]

DMBE II

V° = 5.8472 (0)			
c_1 = −9.8340 (−1)	c_{10} = −6.2814 (−1)	c_{18} = −8.5610 (−2)	c_{26} = 7.5568 (−3)
c_2 = −2.1836 (0)	c_{11} = 3.8207 (−1)	c_{19} = −2.7164 (−2)	c_{27} = −4.4659 (−3)
c_3 = 3.8540 (−1)	c_{12} = 1.0142 (−1)	c_{20} = −1.1228 (−2)	c_{28} = 6.0668 (−3)
c_4 = 3.8215 (−2)	c_{13} = 6.0124 (−3)	c_{21} = 2.7195 (−2)	c_{29} = 2.0637 (−3)
c_5 = 1.9349 (0)	c_{14} = 2.5117 (−2)	c_{22} = −1.5328 (−4)	c_{30} = 1.8701 (−3)
c_6 = −5.5602 (−1)	c_{15} = −5.7318 (−2)	c_{23} = −2.4537 (−3)	c_{31} = −3.9858 (−3)
c_7 = −7.1609 (−2)	c_{16} = −2.0818 (−2)	c_{24} = 1.1601 (−2)	c_{32} = 2.7786 (−3)
c_8 = −7.0660 (−2)	c_{17} = 8.8011 (−2)	c_{25} = 1.3576 (−3)	c_{33} = −2.5483 (−4)
c_9 = 6.5073 (−2)			

$\gamma_0^{(1)}$ = −2.46683 (0) $\gamma_0^{(2)}$ = −1.64300 (0) $\gamma_0^{(3)}$ = −1.64300 (0)
$\gamma_1^{(1)}$ = 0.98202 (0) $\gamma_1^{(2)}$ = 0.62 (0) $\gamma_1^{(3)}$ = 0.62 (0)

DMBE III

V° = 2.0245 (1)			
c_1 = −1.0827 (0)	c_{10} = −4.0323 (−1)	c_{18} = −5.1866 (−2)	c_{26} = 1.8273 (−3)
c_2 = −1.5532 (0)	c_{11} = 2.5285 (−1)	c_{19} = 1.9565 (−3)	c_{27} = −2.7984 (−3)
c_3 = 4.8201 (−1)	c_{12} = −3.3377 (−3)	c_{20} = −4.6763 (−3)	c_{28} = 3.4617 (−3)
c_4 = 9.9026 (−2)	c_{13} = 1.2622 (−2)	c_{21} = 7.6118 (−3)	c_{29} = 1.8739 (−4)
c_5 = 1.2977 (0)	c_{14} = 8.4826 (−3)	c_{22} = −5.8673 (−4)	c_{30} = 9.4458 (−4)
c_6 = −4.0758 (−1)	c_{15} = −1.0826 (−2)	c_{23} = −3.8808 (−4)	c_{31} = −1.1727 (−3)
c_7 = −1.0942 (−1)	c_{16} = 8.0499 (−4)	c_{24} = 2.1401 (−3)	c_{32} = −9.5638 (−4)
c_8 = −5.1977 (−2)	c_{17} = 5.5122 (−2)	c_{25} = −1.3589 (−4)	c_{33} = −3.7996 (−4)
c_9 = −6.5829 (−4)			

$\gamma_0^{(1)}$ = −2.46683 (0) $\gamma_0^{(2)}$ = −1.64300 (0) $\gamma_0^{(3)}$ = −1.64300 (0)
$\gamma_1^{(1)}$ = 0.98202 (0) $\gamma_1^{(2)}$ = 0.62 (0) $\gamma_1^{(3)}$ = 0.62 (0)

[a] Calculated from eq 12; units are as in Table I. [b] Given in parentheses are the powers of 10 by which the numbers should be multiplied, e.g., 5.8472 (0) = 5.8472×10^0.

TABLE VII: Spectroscopic Properties of the Hydroperoxyl Radical (C_s Minima)[a]

property	ab initio[9]	MBE[15,b]	DMBE I[17]	DMBE II	DMBE III	exptl[6,18-21]		
				Geometry				
R_1/a_0	2.58	2.570	2.543	2.584	2.512	2.52	2.57	2.512 ± 0.001
R_2/a_0	1.83	1.861	1.893	1.870	1.843	1.85	1.86	1.843 ± 0.004
R_3/a_0	3.51		3.525	3.530	3.457			
HOO/deg	104.7	106.0	104.28	103.70	104.02	104.1	106	104.02 ± 0.24
				Dissociation Energy				
D_e/E_h	−0.2488	−0.2747	−0.2808	−0.2797	−0.2745			−0.2747 ± 0.003
				Force Constants				
$F_{11}/E_h a_0^{-2}$	0.452	0.375	0.522	0.426	0.375			0.375
$F_{22}/E_h a_0^{-2}$	0.497	0.418	0.329	0.273	0.417			0.418
$F_{12}/E_h a_0^{-2}$	−0.0172	0.0064	0.0264	0.0186	0.0060			0.0064
$F_{\alpha\alpha}/E_h a_0^{-1}$	0.277	0.240	0.445	0.393	0.241			0.240
$F_{1\alpha}/E_h a_0^{-1}$	0.0941	0.0482	0.138	0.116	0.0482			0.0482
$F_{2\alpha}/E_h a_0^{-1}$	−0.0247	−0.0607	0.0068	−0.0202	−0.0600			−0.0607

[a] The dissociation energy, in E_h, is taken relative to the three isolated atoms. R_1 labels the OO bond distance, in a_0. [b] The force field has been fitted to the experimental data reported in this table.

experimentally found for the isolated diatomic fragments, i.e., $\beta_{OO}/\beta_{OH} = 1.15$. Thus, only β_{OH} and $\gamma_1^{(2)} = \gamma_1^{(3)}$ were systematically varied until the isotropic component of the O–OH interaction potential and the O + OH minimum energy path were barrier free. This procedure gave $\beta_{OH} = 1.42a_0^{-1}$ and $\beta_{OO} = 1.633a_0^{-1}$ for the final fit.

The DMBE potential energy surface (denoted hereafter as DMBE II) obtained from the above procedure is numerically defined in Table VI, while the spectroscopic force field it predicts for the hydroperoxyl radical is reported in Table VII. We note the reasonably good agreement with the best available empirical estimates and our own force field data from article I. Moreover, quasiclassical trajectories for the $O + OH \rightarrow O_2 + H$ reaction run on this potential surface have produced thermal rate coefficients in good agreement with the best reported experimental values;[36,49-52] a detailed description of these trajectory calculations as well as those obtained on the DMBE III potential surface reported next will be presented elsewhere.[29]

Although the DMBE II potential surface shows a definite improvement over the ad hoc potential of Melius and Blint,[9] which was fitted to their own ab initio data, it would be desirable for spectroscopic studies to have a HO_2 potential function (DMBE III) that reproduces the experimental quadratic force field reported elsewhere[6,21] for this species. This has been accomplished by having 10 extra conditions imposed (namely, the well depth, three first derivatives, and six quadratic force constants at the HO_2 equilibrium geometry) as further items in the least-squares minimization procedure. For example, a first derivative is considered as an extra data point for which the model function is the gradient of the potential energy surface with respect to a given internuclear coordinate; in the present case, such gradient will be evaluated at the triatomic equilibrium geometry and hence is equal to zero. Thus, we suggest a least-squares fitting procedure where the ab initio energies and the experimental data are dealt with on an equal footing. To ensure that the calculated and experimental values agreed within error bars, we attributed special weights to the various items as summarized in Table V. Since the resulting function showed a tendency to develop nonphysical minima at the strong interaction region where ab initio data points are unavailable, a further point had to be given to guide the potential at such regions. We have estimated this point from the HO_2 DMBE II potential energy surface reported above. In addition, two extra points (numbers 369 and 370 of Table V) were added to prevent the DMBE III potential surface from developing a small barrier (<1 kcal mol^{-1}) at the $H + O_2$ asymptotic channel; the associated energies have also been estimated from the DMBE

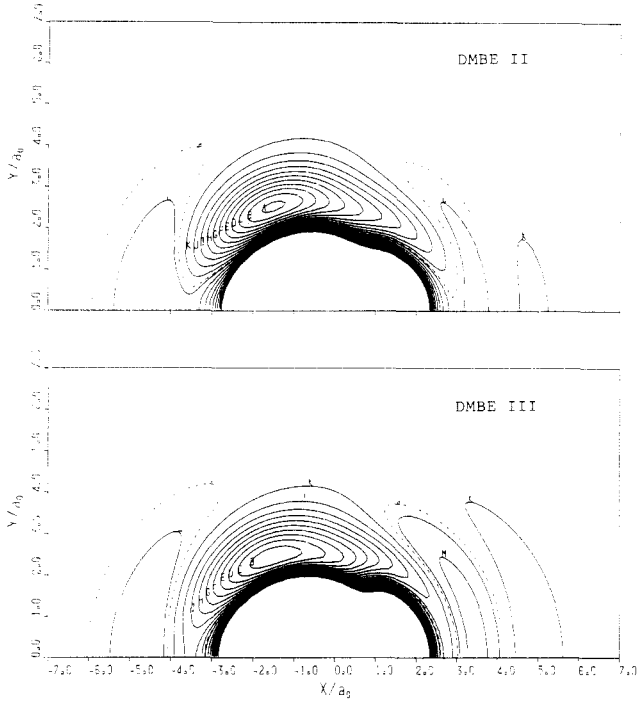

Figure 6. Contour plots for an O atom moving around an equilibrium OH that lies along the x axis with the O end on the negative part of this axis and the center of the bond fixed at the origin. In this figure, as well as in Figure 7, the upper plot refers to the DMBE II potential energy surface, while the other is for the DMBE III potential surface. Contours are equally spaced by 0.01 E_h, starting at $A = -0.277$ E_h. Shown by the dashed line (contour a) is the energy contour corresponding to the O + OH dissociation limit.

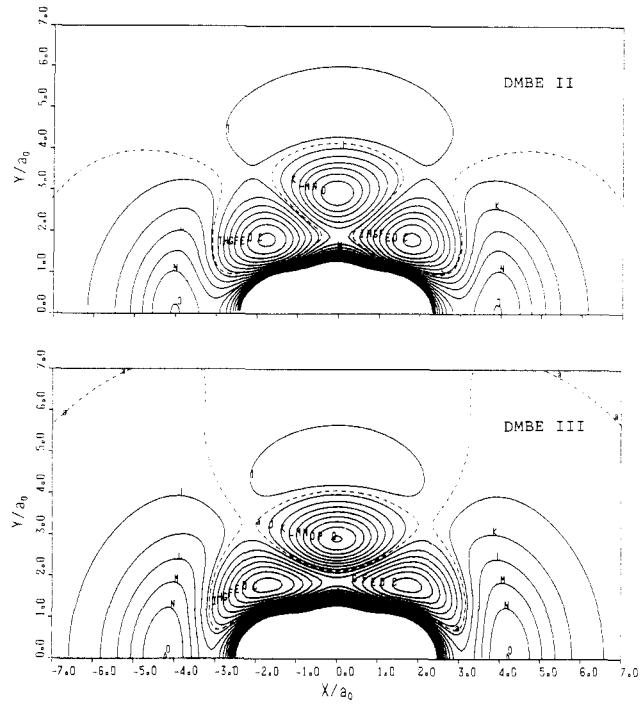

Figure 7. Contour plots for a H atom moving around an equilibrium O_2 molecule with the center of the bond fixed at the origin. Contours are as in Figure 6, except for contour a, which refers now to the H + O_2 dissociation limit.

II potential energy surface from the current work. We conclude this section by reporting the unweighted root-mean-square deviations for the two DMBE potential surfaces with respect to the three-body residual EHF ab initio energies of Melius and Blint: 0.0073 and 0.0121 E_h for the DMBE II and DMBE III potential surfaces, respectively. These values may be compared with those for the ad hoc Melius–Blint[9] form and our previous DMBE I surface,[17] respectively 0.0116 and 0.0073 E_h. Note that the larger root-mean-square deviation for the DMBE III potential surface is mainly due to the form chosen for the weighting function that weights least the ab initio points near the equilibrium HO_2 geometry.

3. Results and Discussion

The HO_2 DMBE (II and III) potential surfaces from the present work are numerically defined in Tables I–III and VI. Note that the coefficients for the three-body electrostatic energy term and the residual three-body EHF term (which are reported in Tables III and VI, respectively) are the only ones that differ from those reported in article I; the coefficients of Tables I and II have therefore been given here only for completeness.

Figure 6 displays equipotential energy contours of the final HO_2 DMBE (II and III) potential surfaces for an O atom moving around an equilibrium OH diatomic. Similar equipotential energy contours but for H moving around an equilibrium O_2 are shown in Figure 7. Note the absence of an energy barrier in the plots of Figures 6 and 7 and hence absent for both O approaching OH and H approaching O_2.

In Figure 8 we show equipotential energy contours for the OO and OH stretching in HO_2 with the HOO angle kept fixed at the corresponding equilibrium value, while Figure 9 shows contours for the stretching of the two OH bonds in linear OHO. Apparent from Figure 9 are the two minima associated with the OH···O and O···HO equivalent hydrogen-bonded structures. Note, however, that the seemingly $D_{\infty h}$ minimum at short OH distances is an artifact of the dimensionality of the graphical representation being truly a saddle point for the motion of O around the H end of OH. Despite the similar topographies of the DMBE II and DMBE III potential surfaces at these regions of configuration space, they show some noticeable differences, particularly concerning the height of the barrier for the O + OH → OH + O H atom exchange reaction. Accurate ab initio calculations for the H atom migration between the two O atoms would therefore provide an important way of settling this issue.

Figure 10 shows contours for the C_{2v} insertion of H into O_2. Again, the DMBE II and DMBE III potential surfaces show some quantitative differences mainly near the collinear O–H–O geometries referred to in the previous paragraph.

Figures 11 and 12 show the leading terms in the Legendre analysis of the O–OH and H–O_2 interaction potentials with the diatomics kept fixed at their equilibrium geometries, while Figure 13 compares the V_0 for the O–OH interaction with that obtained from other treatments. Again, we have reported the results obtained from both the HO_2 DMBE II and III potential surfaces. Note the absence of a positive barrier in the spherically symmetric component of the O–OH interaction potential for both the DMBE II and Melius–Blint potentials; see also Figure 5. For the HO_2 DMBE III potential energy surface this barrier exists, though it is small. Note especially that the condition of no barrier in V_0 (or, if existing, a small barrier) has been considered in the present work a key feature for a good O + OH dynamics.

The properties of the C_s chemical minima for both the HO_2 DMBE II and III potential energy surfaces are gathered in Table VII. Also shown for comparison in this table are the attributes of the HO_2 DMBE I potential surface,[17] those of the Melius–Blint[9] ad hoc functional form, and the experimental values.[18-21] Particularly striking is the good agreement between the properties from potential II and experiment. Table VIII summarizes the properties of other stationary points in the HO_2 ground-state potential energy surface. It is seen that all relevant chemical structures associated with stationary points in article I remain in the new potential, although they differ somehow quantitatively.

4. Concluding Remarks

The properties of the HO_2 DMBE potentials derived in the present work have been carefully analyzed by numerical methods and by graphical techniques. Whenever available, experimental information has been used to parametrize the present functions. In addition, a least-squares fitting procedure has been adopted

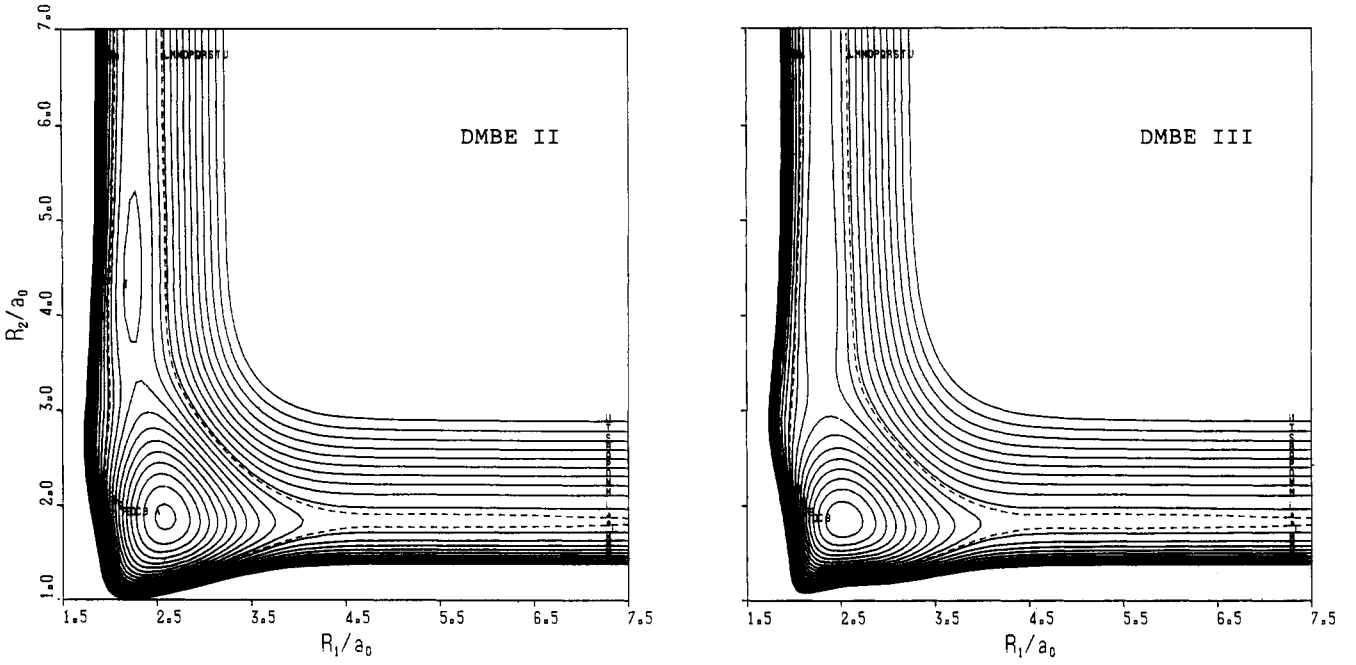

Figure 8. Contour plots for the stretching of the OO and OH bonds in $HO_2(\tilde{X}^2A'')$ with the HOO angle fixed at 103.7°. In this figure, as well as in Figures 9–12, the plot in the left-hand side refers to the DMBE II potential energy surface, while the other is for the DMBE III potential surface. Contours are as in Figure 6.

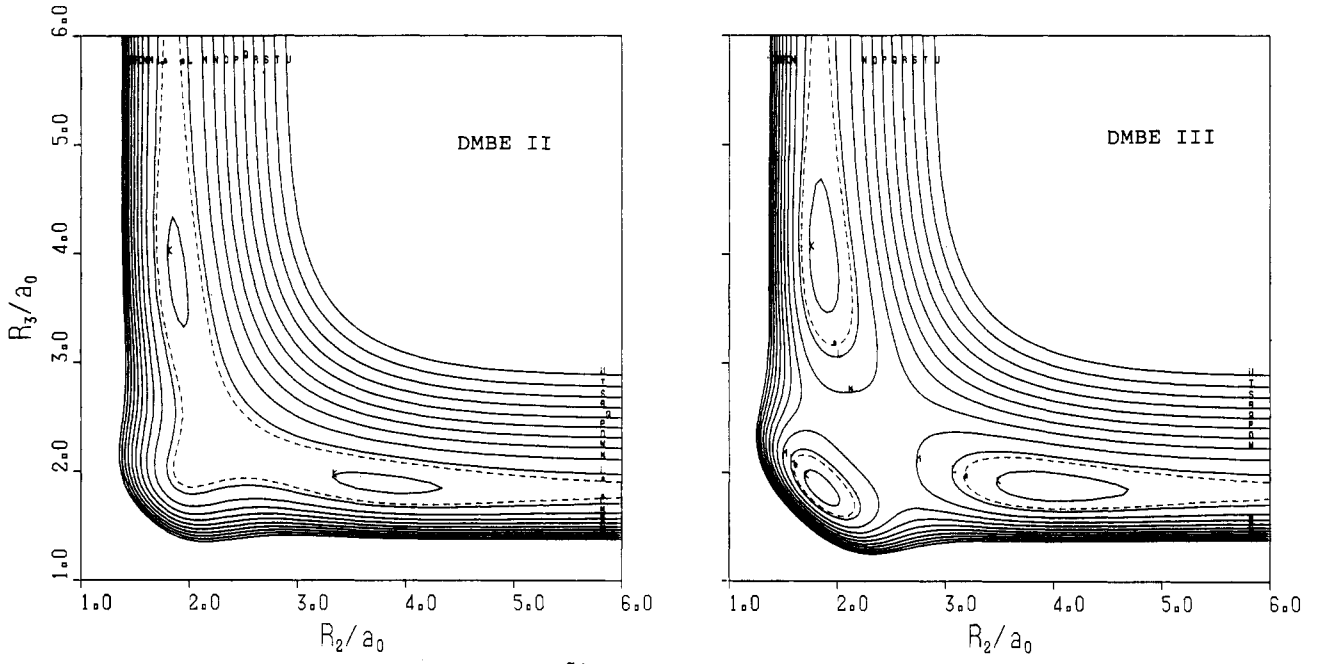

Figure 9. Contours for the stretching of the OH bonds in OHO $(\tilde{X}^2A'')$ showing the two equivalent OH···O and O···HO hydrogen-bonded structures. Contours are as in Figure 6.

to derive the HO_2 DMBE III potential energy surface that takes the ab initio energies of Melius and Blint[9] and the available experimental spectroscopic force field data for the hydroperoxyl radical[6,18-21] on an equal footing, perhaps yielding the most realistic global representation currently available for that surface.

The HO_2 DMBE II and III potentials derived in this work have also been used for extensive quasiclassical trajectory calculations of the O + OH → O_2 + H reaction with good success. Since a detailed description of these calculations is presented elsewhere,[29] we refer to only the results for the thermal rate constant at T = 500 and 2000 K based on the HO_2 DMBE III potential surface. At T = 500 K one gets $k(500)$ = 1.55 (±0.12) × 10^{13} cm^3 mol^{-1} s^{-1}, a result that is in good agreement with the best available experimental estimates[49,50] (1.45 (±0.05) × 10^{13} and 1.68 (±0.06) × 10^{13} cm^3 mol^{-1} s^{-1}, respectively), while at T = 2000 K one obtains $k(2000)$ = 8.58 (±0.10) × 10^{12} cm^3 mol^{-1} s^{-1}, which is in reasonably good agreement with the experimental correlation of Cohen and Westberg[36] ($k(2000)$ = 1.02 (±0.36) × 10^{13} cm^3 mol^{-1} s^{-1}) but somewhat too low in comparison with the most recent estimate of Frank and Just[52] ($k(2000)$ = 1.39 (±0.38) × 10^{13} cm^3 mol^{-1} s^{-1}).

Neither the DMBE II nor DMBE III potential energy surfaces from the present work explicitly treat all the fine-structure states of O(^{3}P) + OH($^2\Pi$). Indeed, no representations so far published for this system have done so, including one[54] that has just recently appeared. Quantum mechanically, this can be done by a Gentry–Giese[55] type analysis of the long-range force which when applied to O + OH produces a matrix of 36 states. The diagonalization of this matrix as a function of angle of approach and

(54) Lemon, W. J.; Hase, W. L. *J. Phys. Chem.* **1987**, *91*, 1596.
(55) Gentry, W. R.; Giese, C. F. *J. Chem. Phys.* **1977**, *67*, 2355.

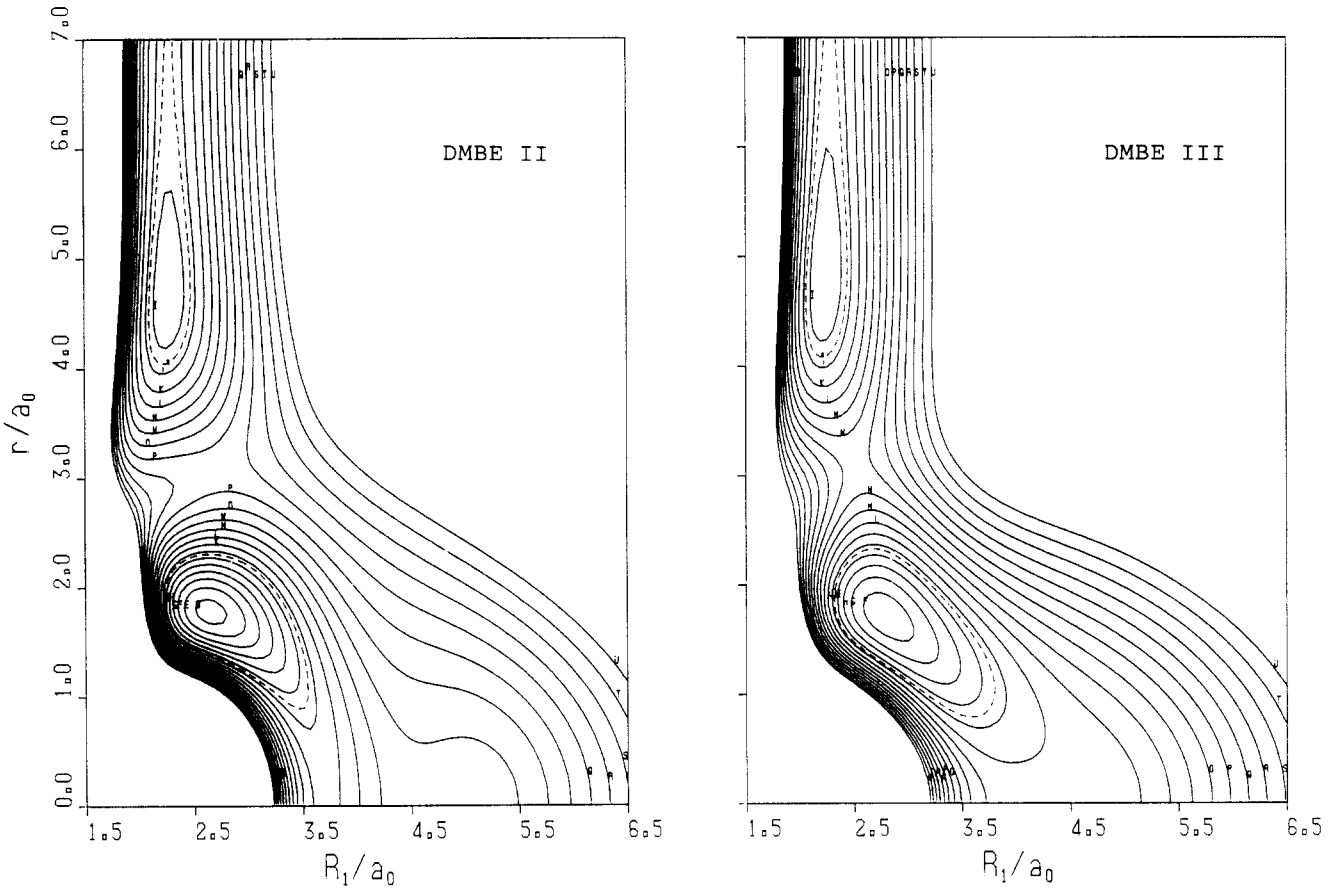

Figure 10. Contour plots for the C_{2v} insertion of H into O_2. Contours are as in Figure 7.

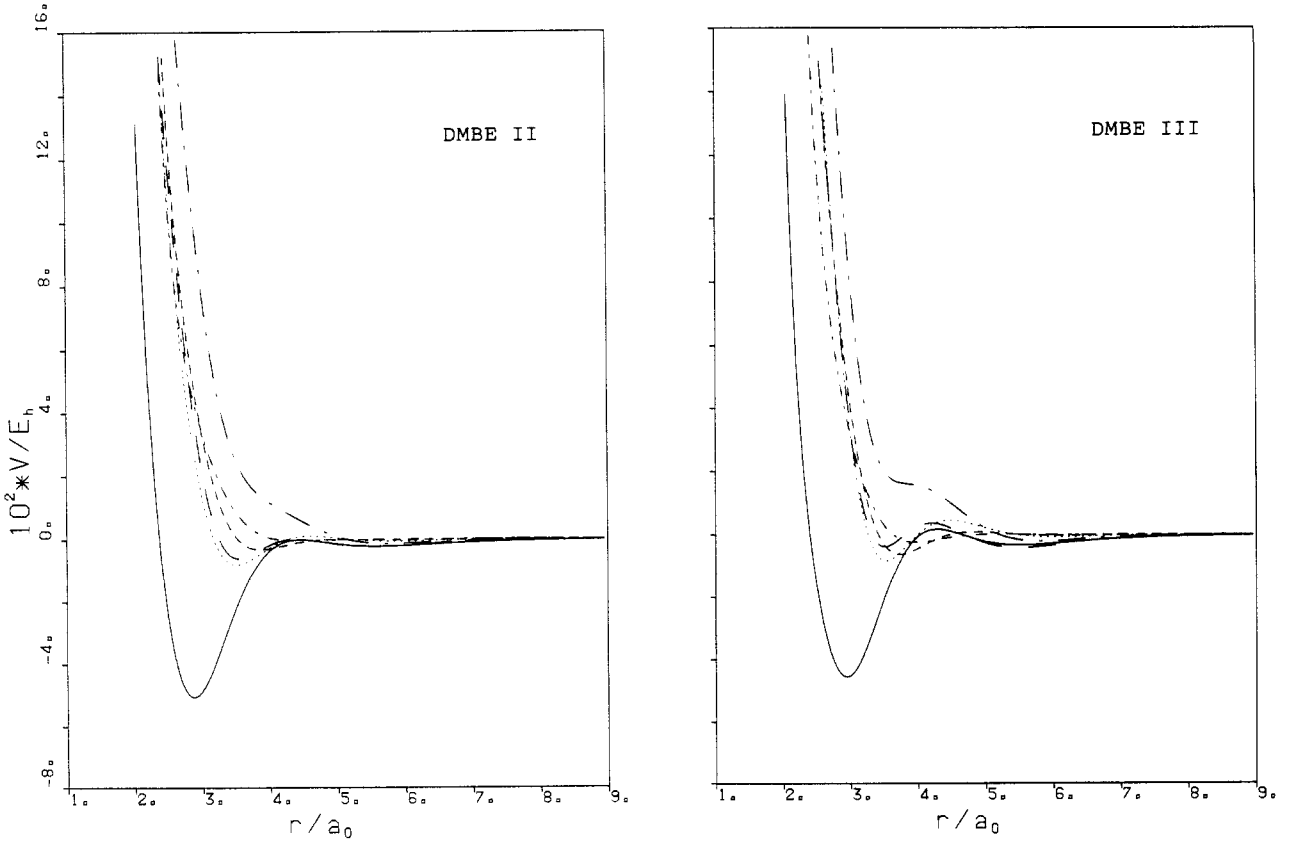

Figure 11. Isotropic (V_0) and anisotropic (V_1, V_2, V_3, V_4, and V_5) components of the O–OH interaction potential, with the molecule fixed at the equilibrium diatomic geometry, for $1 \leq r \leq 9$ a_0. Note that r is now the distance from the O atom to the center of mass of OH: (—) V_0; (– – –) V_1; (–·–) V_2; (···) V_3; (– · –) V_4; (·· –) V_5.

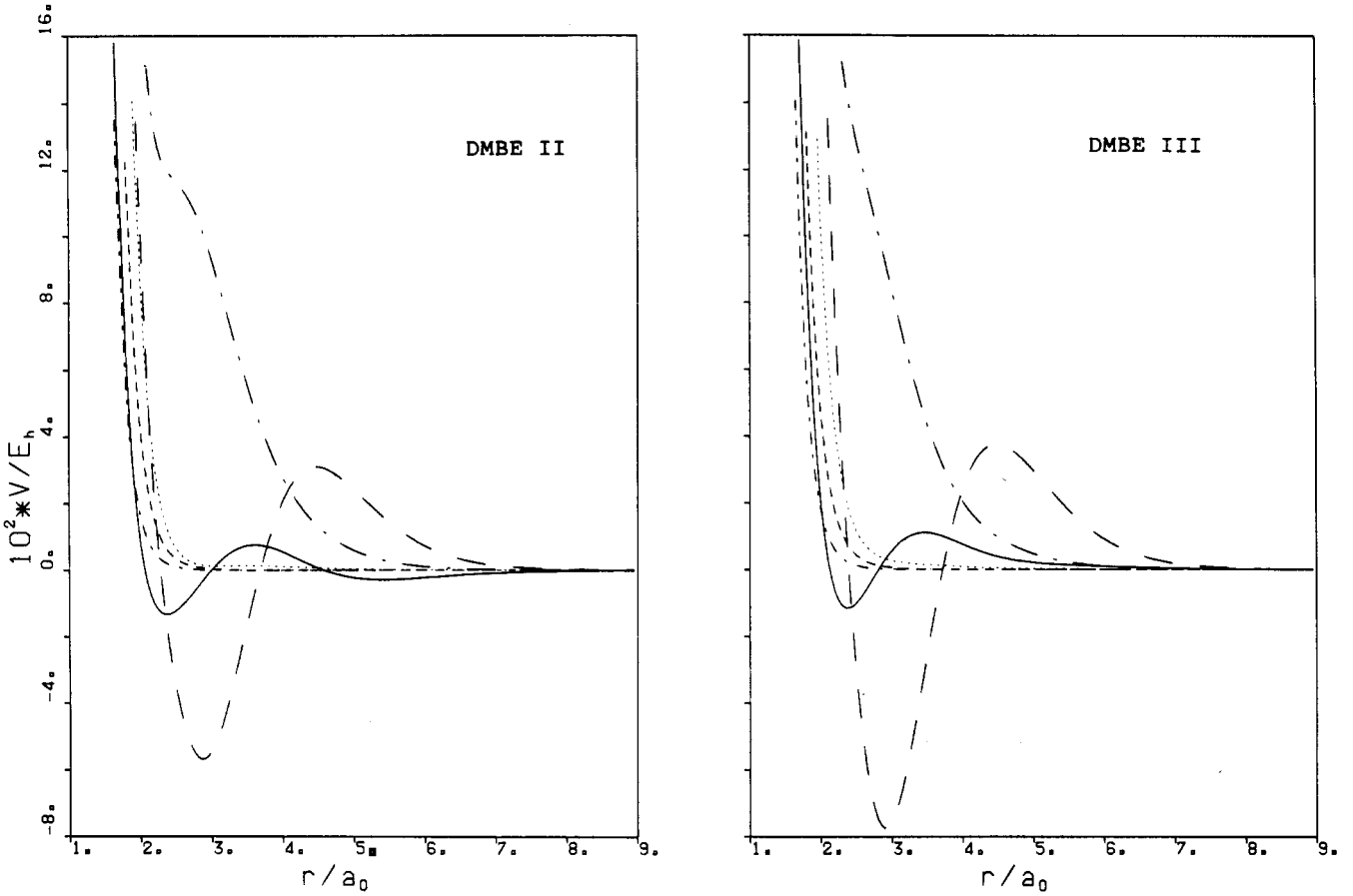

Figure 12. Isotropic (V_0) and anisotropic (V_2, V_4, V_6, V_8, and V_{10}) components of the H–O_2 interaction potential, with the molecule fixed at the equilibrium diatomic geometry, for $1 \leq r \leq 9\ a_0$: (—) V_0; (– – –) V_2; (–·–) V_4; (···) V_6; (– · –) V_8; (– ·· –) V_{10}.

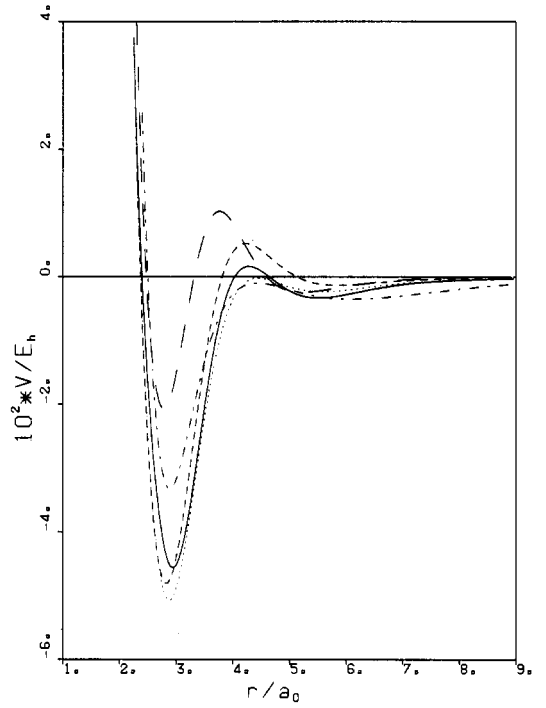

Figure 13. Comparison of V_0 for the O–OH interaction with that obtained from other models. Symbols are as in Figure 5.

distance of O from OH yields[35] 18 doubly degenerate potential energy surfaces that include the coupling and the quadrupole axis orientation effects mentioned in section 2.1; the lowest doubly degenerate potential energy surface so obtained is therefore the adiabatic potential that should go smoothly to the Melius–Blint electronic structure calculations. Yet, although spin–orbit coupling may be important and should ultimately be included in any representation of the O + OH interaction, it is also possible that for calculations of thermal rate constants and other macroscopic observables an explicit treatment of spin–orbit coupling may be

TABLE VIII: Geometries and Energies of the Metastable Minima and Saddle Points Predicted by the DMBE Potentials for the $H + O_2 \rightarrow OH + O$ and Isomerization Reactions[a]

property	DMBE I[17]	DMBE II	DMBE III
T-Shaped H–O_2 Structure			
R_1/a_0	2.243	2.230	2.267
R_2/a_0	4.927	4.932	4.824
R_3/a_0	4.927	4.932	4.824
HOO/deg	76.84	76.94	76.41
V/E_h	−0.2012	−0.2050	−0.2039
Hydrogen-Bonded OH···O Structure			
R_1/a_0	5.824	5.680	5.808
R_2/a_0	1.875	1.888	1.863
R_3/a_0	3.949	3.792	3.945
HOO/deg	0	0	0
V/E_h	−0.1796	−0.1784	−0.1807
Saddle Point Structure for the H + O_2 Reaction			
R_1/a_0	2.284	2.268	2.289
R_2/a_0	3.529	3.547	3.426
R_3/a_0	4.702	4.730	4.648
HOO/deg	106.00	106.80	107.16
V/E_h	−0.1925	−0.1967	−0.1921
Saddle Point Structure for the HO_2 Isomerization			
R_1/a_0	2.749	2.783	2.641
R_2/a_0	2.192	2.212	2.217
R_3/a_0	2.192	2.212	2.217
HOO/deg	51.16	51.01	53.45
V/E_h	−0.2257	−0.2332	−0.2509

[a] Energies, in E_h, are taken realtive to three isolated atoms.

unnecessary.[35] Moreover, Wagner[35] has shown for O + OH → HO_2 recombination that spin-orbit coupling may be correctly incorporated into the calculation of the thermal rate constant by a Boltzmann term involving the energies and degeneracies of the $O(^3P)$ and $OH(^2\Pi)$ sublevels.

Finally, we make a brief comment on an interesting approach to the potential function of the hydroperoxyl radical that appeared after this work was completed. Lemon and Hase[54] suggest a switching function formalism and extensions of BEBO[56] concepts in a manner that may enable one to relate potential energy surface properties to dynamical and kinetic attributes of the HO_2 system. Note, however, that their function neither describes H atom migration between the oxygen atoms nor shows the correct R^{-n} dependence at the asymptotic channels. Moreover, as they have pointed out, the transition state for the H + O_2 → O + OH reaction is expected to have an intermediate OO distance,[57] a distance shorter than those for which the potential is accurately represented by long-range R^{-n} forces and a distance longer than those for which the potential is accurately represented by the Morse function. At such distances, ab initio studies of the O + OH minimum energy path are difficult,[58] and hence the interpolation scheme suggested by the DMBE method may reveal itself as a very useful one in such circumstances.

Acknowledgment. We gratefully acknowledge very helpful correspondence with Dr. Albert Wagner of Argonne National Laboratory (U.S.A.). Financial support from the Instituto Nacional de Investigação Científica (INIC), Lisbon, is also gratefully acknowledged. This project has also benefitted from a Portuguese-Spanish joint venture (Acção Integrada). L.A.M.Q. thanks the Ministerio de Educacion y Ciencia, Spain, for an F.P.I. grant and the University of Salamanca for leave of absence.

Registry No. HO_2, 3170-83-0; O, 17778-80-2; OH, 3352-57-6.

(56) Johnston, H. S. *Gas-Phase Rate Theory*; Ronald: New York, 1966; p 55.
(57) Hase, W. L.; Duchovic, R. J. *J. Chem. Phys.* **1985**, *83*, 3448.
(58) Carsky, P.; Svrcek, M.; Hubac, I.; Brown, F. B.; Shavitt, I. *Chem. Phys. Lett.* **1982**, *85*, 17.

Some Excited-State Properties of 4-(9-Anthryl)-*N*,*N*,2,3,5,6-hexamethylaniline

W. Baumann,* B. Schwager, N. Detzer,

Institute of Physical Chemistry, University of Mainz, D65 Mainz, West Germany

T. Okada, and N. Mataga

Department of Chemistry, Faculty of Engineering Science, Osaka University, Toyonaka, Osaka 560, Japan
(Received: August 26, 1987; In Final Form: November 23, 1987)

From the effect of an electric field on the fluorescence, the dipole moment of 4-(9-anthryl)-*N*,*N*,2,3,5,6-hexamethylaniline in its polar fluorescent excited state could be determined in several solvents. Its value of 60 × 10^{-30} C m was found to be solvent independent.

Introduction

4-(9-Anthryl)-*N*,*N*-dimethylaniline (ADMA) and some of its derivatives show an absorption spectrum very similar to that of anthracene. At a closer view, a long-wavelength shoulder has been detected and interpreted as a charge-transfer absorption by Mataga's group.[1-3] From kinetic investigations of the fluorescence of ADMA it was concluded[4,5] that an excited intramolecular charge-transfer (ICT) state is formed spontaneously after excitation to a locally excited anthracene-like state where the anthryl and dimethylamino moieties are perpendicular. Grabowski[6,7] introduced the term "twisted intramolecular charge-transfer (TICT) state" for this kind of excited state, which have been reviewed quite recently by Rettig.[8] The fluorescence behavior of these compounds in solvents of medium polarity then must be assumed to be due to a superposition of fluorescence from a TICT state and from another state, perhaps a locally excited state. On the other hand, in 1979 Baumann et al. tried to explain the spectroscopic behavior especially in electric fields by one emitting state only. This interpretation then yielded large polarizabilities in this excited state.[9] Interpretations assuming only one emitting state with ADMA that changes its electronic and geometrical structure depending on the solvent polarity or assuming the existence of the "multiple kinds of structures" in the intramolecular CT state of ADMA depending on the interaction with solvent molecules have also been proposed on the basis of fluorescence and S_n-S_1 transient absorption measurements.[3,10]

For more insight into the nature of the excited fluorescent states or states and/or conformers, two new sterically hindered molecules have been synthesized, namely, 4-(9-anthryl)-*N*,*N*,2,3,5,6-hexamethylaniline (TM-ADMA) and 4-(9-anthryl)-*N*,*N*,2,6-tetramethylaniline (2,6-DM-ADMA).[11] Due to sterical hindrance, with TM-ADMA both the anthryl and the dimethylamino subunits are twisted out of the phenyl plane by at least 60°; with 2,6-DM-ADMA only the dimethylamino group is twisted.

In this paper, the results from the measurements on the solvent dependence of the integral electrooptical emission measurements and the S_n-S_1 absorption spectra of these compounds are discussed.

Experimental Section

Integral Electrooptical Emission Measurements. With integral electrooptical emission measurements (IEOEM) the effect of an

(1) Ide, R.; Sakata, Y.; Misumi, S.; Okada, T.; Mataga, N. *J. Chem. Soc., Chem. Commun.* **1972**, 1009.
(2) Okada, T.; Fujita, T.; Kubota, M.; Masaki, S.; Mataga, N.; Ide, R.; Sakata, Y.; Misumi, S. *Chem. Phys. Lett.* **1972**, *14*, 563.
(3) Okada, T.; Fujita, T.; Mataga, N. *Z. Phys. Chem. (Neue Folge)* **1976**, *101*, 57.
(4) Siemiarczuk, A.; Grabowski, Z. R.; Krȏwczynski, A.; Asher, M.; Ottolenghi, M. *Chem. Phys. Lett.* **1977**, *51*, 315.
(5) Siemiarczuk, A.; Koput, J.; Pohorille, A. *Z. Naturforsch., A: Phys., Phys. Chem., Kosmophys.* **1982**, *37*, 598.
(6) Grabowski, Z. R.; Rotkiewicz, K.; Siemiarczuk, A. *J. Lumin.* **1979**, *18/19*, 420.
(7) Grabowski, Z. R.; Rotkiewicz, K.; Kiemiarczuk, A.; Cowley, D. J.; Baumann, W. *Nouv. J. Chim.* **1979**, *3*, 443.
(8) Rettig, W. *Angew. Chem.* **1986**, *98*, 969.
(9) Baumann, W.; Petzke, F.; Loosen, K.-D. *Z. Naturforsch., A: Phys., Phys. Chem., Kosmophys.* **1979**, *34*, 1070.
(10) Okada, T.; Kawai, M.; Ikemachi, T.; Mataga, N.; Sakata, Y.; Misumi, S.; Shionoya, S. *J. Phys. Chem.* **1984**, *88*, 1976.
(11) Detzer, N.; Baumann, W.; Schwager, B.; Fröhling, J.-C.; Brittinger, C. *Z. Naturforsch., A: Phys., Phys. Chem., Kosmophys.* **1987**, *42*, 395.

0022-3654/88/2092-3742$01.50/0